AN ABSTRACT OF THE THESIS OF

Levi A. Sitts for the degree of Honors Baccalaureate of Science in Mechanical Engineering presented on May 30, 2012. Title: Direct Numerical Simulation of a Low-Reynolds-Number Flat-Plate Airfoil with a Passively Actuated Trailing-Edge Flap

Abstract approved:

Sourabh Apte

Direct numerical simulation was applied to a two dimensional cross section of a flat-plate airfoil with a passively actuated trailing-edge flap. The flap consisted of 30% of the chord length. Tests were performed at a Reynolds number of 1000, and a pitch angle of 5 degrees. The airfoil underwent a sinusoidal plunging motion to simulate a flapping wing. The fluid-structure interaction was modeled by the second-order fictitious domain approach by Apte et al. [1], and the flap was regarded as a spring-mounted compound pendulum. Verification tests were performed for cases of static and spring-mounted cylinders at a Reynolds number of 200. It was observed that the amplitude of the flap oscillations about the hinge increased as the natural frequency approached the plunging frequency. For natural frequencies lower than or equal to the plunging frequency, the average drag coefficient over time was *negative*, meaning that these cases produced a net thrust. This trend is opposite of the results obtained by Apte [2], for a very similar situation, at Re=14700. Either the differences in the viscous effects or the slight changes in wing thickness (or both) might be responsible for this discrepancy.

Key Words: Direct Numerical Simulation; Low Reynolds Number; Micro Air Vehicle; Thin Airfoil; Passive Actuation

Corresponding e-mail address: levisitts@gmail.com

Direct Numerical Simulation of a Low-Reynolds-Number Flat-Plate Airfoil with a Passively Actuated Trailing-Edge Flap

by

Levi A. Sitts

A PROJECT

submitted to

Oregon State University

University Honors College

in partial fulfillment of
the requirements for the
degree of

Honors Baccalaureate of Science in Mechanical Engineering (Honors Associate)

Presented May 30, 2012
Commencement June 17, 2012

Honors Baccalaureate of Science in Mechanical Engineering project of Levi A. Sitts presented on May 30, 2012.

APPROVED:

Mentor, representing Mechanical Engineering

Committee Member, representing Mechanical Engineering

Committee Member, representing Mechanical Engineering

Head, School of Mechanical, Industrial, and Manufacturing Engineering

Dean, University Honors College

I understand that my project will become part of the permanent collection of Oregon State University, University Honors College. My signature below authorizes release of my project to any reader upon request.

Levi A. Sitts, Author

ACKNOWEDGEMENTS

I would like to thank my mentor, Dr. Sourabh Apte, for his patience and guidance throughout the research process.

Thank you, also, to Kevin Drost and Joseph Skitka for their help in learning how to use the solver and tecplot360.

TABLE OF CONTENTS

LIST OF FIGURES

LIST OF TABLES

LIST OF APPENDIX FIGURES

DEDICATION

To my loving fiancée, Dana Pace.

Direct Numerical Simulation of a Low-Reynolds-Number Flat-Plate Airfoil with a Passively Actuated Trailing-Edge Flap

INTRODUCTION

Background

The study of low-Reynolds-number airfoils has gained considerable momentum in recent years, due to the increasing use of micro air vehicles (MAVs). MAVs span a wide spectrum of sizes, shapes, and capabilities, ranging from military applications to children's toys. Understanding the behavior of low-Reynolds-number airfoils is an important step in designing more effective MAVs.

The Reynolds number (Re) of an airfoil is a dimensionless quantity defined in terms of the chord length (c), free-stream velocity (U_∞), and kinematic viscosity (ν) of the surrounding fluid. The fundamental relationship between these variables is given by equation (1).

$$\mathrm{Re} = \frac{U_\infty c}{\nu} \tag{1}$$

Traditionally, airfoils with Reynolds numbers less than 10^5 are considered low-Reynolds-number airfoils [3]. The physical interpretation of the Reynolds number can be thought of as the relative importance of inertial forces to viscous forces within the flow. Large Reynolds numbers would indicate that the flow is dominated by inertial forces, such as momentum. At low Reynolds numbers, viscous forces determine the major flow characteristics, and smooth fluid motion is typically observed.

Many MAVs utilize simple, flat-plate, airfoils. To achieve reasonable lift at low Reynolds numbers, flat-plate airfoils might require high angles of attack. Under these conditions, thin airfoils are especially susceptible to flow separation at the leading edge which can give rise to dynamic stall. In fact, the term “thin-airfoil stall”, as defined by McCullough and Gault [4], is “flow separation at the leading edge with reattachment at a point that moves progressively rearward with increasing angle of attack”. This “separation bubble” can lead to highly sporadic lift and drag forces on the wing, making it difficult to control the aircraft. To mitigate this problem, a leading-edge flap can be installed to, effectively, add camber to the wing and delay separation. A study by Drost [3] found that the addition of a leading-edge flap can have a positive impact on the lift and drag characteristics of thin airfoils. Several cases were studied, both for static and oscillating leading-edge flap scenarios.

A report by Apte [2] investigated the addition of both a leading- and trailing-edge flap (separately) on a thin, plunging, airfoil. Results suggest that a passively controlled (i.e., spring loaded) flap on the leading or trailing edge of a thin airfoil can help yield significant improvements in flight characteristics and may even produce thrust, for the case of a trailing-edge flap.

Objectives

It is the aim of the present study to expand on the previous work by Apte (above), by investigating the effectiveness of a passively actuated trailing-edge flap, at a Reynolds number of 1000 (compared to 14700 as studied by both Apte and Drost). Results will be analyzed for differences between static flap and passive flap scenarios. Of primary interest would be changes in overall lift and drag coefficients of the airfoil between these cases. Figure 1 shows a diagram of a thin airfoil with elliptical leading and trialing edges, at an angle of attack (α) and flap displacement angle (θ).

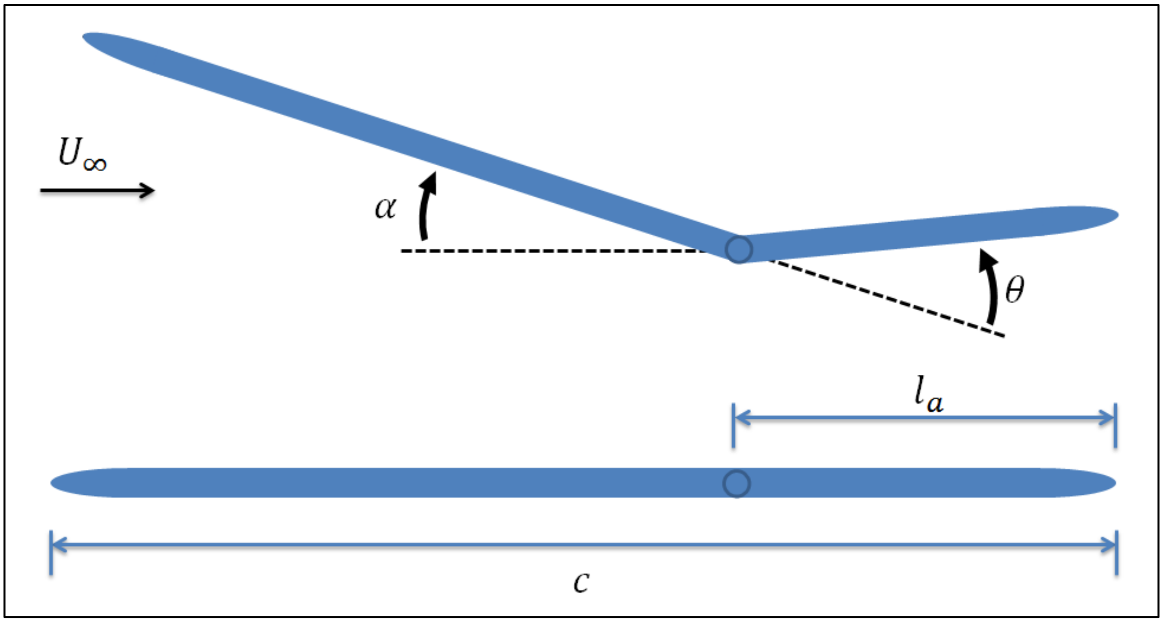

Figure 1: Conceptual side-view diagram of a thin airfoil with a trailing-edge flap. U_∞ *is the velocity of the surrounding fluid,* α *is the pitch angle,* θ *is the flap displacement angle,* c *is the chord length, and* l_a *is the flap length (0.3c).*

Literature Review

Several numerical simulations of flat airfoils have been conducted in the past. A study by Taira and Colonius [5] investigated the effects of three-dimensional flows around low-aspect-ratio flat-plate wings at Reynolds numbers of 300 and 500. Their findings showed that aspect ratio and angle of attack have a large impact on the forces experienced by the immersed body. Depending on the aspect ratio and angle of attack, the wake reached one of three states: (1) steady, (2) periodic unsteady, or (3) aperiodic unsteady. The aperiodic unsteady situation was caused by strong interactions between the leading-edge, trailing-edge, and tip vortices.

Kim and Choi [6] studied the flow around an arbitrarily moving body using an immersed boundary method. Their approach was based on a finite volume method with a staggered mesh arrangement. Forced motion of a circular cylinder was investigated, as well as a freely falling sphere and cube. Results agreed well with previous numerical and experimental evidence.

Uranga et al. [7] worked on predicting the formation of laminar separation bubbles and how they relate to flow transition. Implicit Large Eddy Simulations (LES) were used along with a high-order Discontinuous Galerkin (DG) method. Their work focused on the flow around an SD7003 rectangular wing section at a low angle of attack and Reynolds numbers of 10,000 and 60,000. Their findings were in agreement with published results, despite the course grid employed in their simulations.

Alonso et al. [8] presented "an implicit approach to the solution of the unsteady two-dimensional Navier-Stokes equations", wherein coupled, implicit, non-linear equations were solved iteratively. Results were obtained for the unsteady vortex shedding behind a circular cylinder and for a pitching NACA 64A010 airfoil.

The hovering aerodynamics of flexible flapping wings at resonance were simulated in three dimensions by Masoud and Alexeev [9] via a hybrid computational approach which combined the lattice Boltzmann model (LBM) and the lattice spring model (LSM) for the dynamics of incompressible viscous fluids and the mechanics of elastic solids, respectively. Simulations showed that large amplitude sinusoidal oscillations drastically improved the aerodynamic efficiency of flexible wings at low Reynolds numbers.

Measurements by Broeren and Bragg [10] showed a correlation between the airfoil stall type, as defined by McCullough and Gault [4], and the low frequency oscillation of a LRN-1007 airfoil at a Reynolds number of 300,000. The measurements showed an interaction between the leading-edge separation bubble and the trailing-edge separation as the airfoil oscillates in and out of stall.

Visbal et al. [11] employed a high-fidelity, implicit, large eddy simulation approach to investigate several aspects of the complex flow physics encountered by MAVs. The boundary layer transition of a stationary SD7003 airfoil at Reynolds numbers of 10^4-10^5 and pitch angles of 2˚-14˚were investigated, as well as the unsteady low-Reynolds-number flow past a plunging airfoil.

The study by Drost [3], which was an earlier project conducted under the mentorship of Apte, simulated the flow around a thin airfoil with a movable leading-edge flap. Direct Numerical Simulation (DNS) was used to fully resolve the flow characteristics around the airfoil, using a fictitious domain approach to represent the airfoil surface. Simulations were conducted at a Reynolds number of 14700, and an angle of attack of 20˚. The lift and drag forces on the wing were analyzed for several frequencies of forced flap oscillation. The fluid forces were found to be highly dependent on the vortex shedding at the leading edge, and consequently the oscillatory motion of the flap. Lift and drag forces became more predictable with the use of a leading-edge flap.

Lastly, the recent work by Apte [2] suggests that a trailing-edge flap also has the potential to produce beneficial results for the lift and drag of a thin airfoil. Flow over a plunging airfoil at 10 Hz and 5˚ angle of attack was studied, along with other configurations that included a leading-edge flap. Regarding the simulations of a passive trailing-edge flap, it was found that spring natural frequencies (of the spring-flap system) higher than the plunging frequency of the airfoil lead to a net increase in thrust. As noted in the objectives section, these simulations were conducted at Re=14700. The present study aims to conduct similar trials at a Reynolds number of only 1000.

METHODOLOGY

Numerical Scheme

To solve the fluid structure interaction problem, a second-order fictitious domain approach by Apte et al. [1] was employed on a fixed Cartesian grid. In this approach, the entire fluid-particle domain is assumed to be an incompressible, yet variable density fluid. Inside the "rigid body" region, the fluid is constrained to undergo rigid body motion, while the fluid outside is constrained to be divergence-free. Since the rigid body is undergoing translational and rotational motions, a method of tracking which control volumes (CVs) are inside of the body is required. This is done using a hybrid Lagrangian-Eulerian (HLE) method, wherein material points on the surface of the object are tracked at each time step. The material points start at user-defined locations on the grid, and are then either subjected to user defined velocity constraints (forced plunging on main portion of wing), or allowed to respond passively to the surrounding fluid forces (tail flap passive motion). In both cases, the CVs that happen to contain the material points are tagged as the material boundary.

The flow variables, such as pressure, density, etc., are stored at the CV centers, with the exception of the face-normal velocities, which are stored at the center of the cell faces [1]. The storage variables are staggered in time, such that the velocities and forces are stored at each times step, but pressure, density, and volume fraction are taken at each half time step. A temporally staggered grid arrangement, such as this, provides the benefit of a symmetric discretization, which helps to conserve properties within the numerical scheme.

Governing Equations

The mathematical model used to approximate the behavior of the flap is a second-order ordinary differential equation for a spring-mounted compound pendulum. The free-body diagram depicting this situation is illustrated in Figure 2.

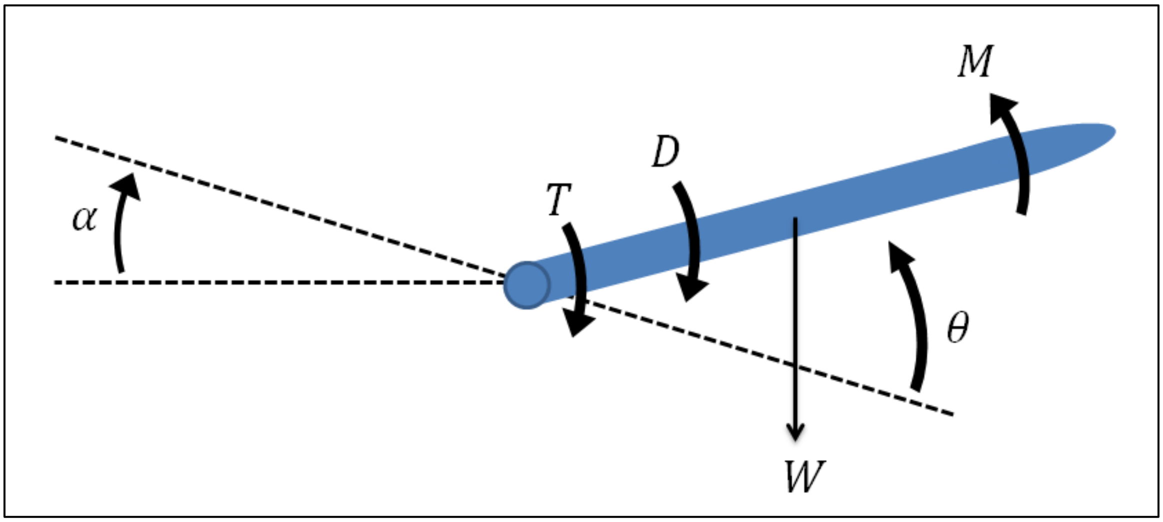

Figure 2: Free-body diagram of tail flap. The figure shows the flap with an elliptical end, but it was actually approximated as a thin rectangle for simplicity.

Here, T represents the Torque due to the spring displacement, D represents the damping moment, M represents the moment caused by fluid forces, and W represents the weight of the flap (approximated as acting at one half of the flap length). α and θ are the wing angle of attack and flap displacement angle, respectively (counter-clockwise positive). The equation of angular motion for this system can be written as follows (assuming a constant angle of attack):

$$\sum M_{hinge} = M - T - D - W\frac{l_a}{2}\cos(\alpha+\theta) = I\frac{d^2\theta}{dt^2} \tag{1.2}$$

Where:

$$M = \tfrac{1}{2} C_M \rho_f U_\infty^2 l_a^2 w \tag{1.3}$$

$$T = K\theta \tag{1.4}$$

$$D = C\frac{d\theta}{dt} \tag{1.5}$$

$$W = mg \tag{1.6}$$

$$I = \tfrac{1}{3} m l_a^2 \tag{1.7}$$

In these equations, C_M represents the pitching moment coefficient due to the fluid forces on the flap, ρ_f represents the density of the fluid, U_∞ is the velocity of the surrounding fluid, l_a is the length of the flap, w is the width of the flap, K is the spring stiffness parameter, C is the damping coefficient, m is the mass of the flap, g is the gravitational constant, and I is the flap moment of inertia about the hinge (approximated as a thin rectangular plate). Substituting equations (1.3) through (1.6) into equation (1.2) yields an expanded form of the equation of motion. After subsequent rearrangement of terms, the equation may be presented in the following form:

$$\frac{d^2\theta}{dt^2} + \frac{C}{I}\frac{d\theta}{dt} + \frac{K}{I}\theta + \frac{mgl_a}{2I}\cos(\alpha + \theta) = \frac{C_M}{I} \tag{1.8}$$

In order to non-dimensionalize this equation, the following substitutions are made:

$$t = \frac{\tau l_a}{U_\infty} \tag{1.9}$$

$$C = 2\xi\sqrt{KI} \tag{1.10}$$

Where τ is a non-dimensional time and ξ is a non-dimensional damping parameter. To further simplify the equation, the following definitions of the Strouhal number

$\left(St_N = f_N l_a / U_\infty\right)$ and spring natural frequency $\left(f_N = \frac{1}{2\pi}\sqrt{K/I}\right)$ are utilized. The final version of the non-dimensional equation can be written as:

$$\frac{d^2\theta}{d\tau^2} + 4\pi\xi St_N \frac{d\theta}{d\tau} + (2\pi St_N)^2\theta + \frac{3gl_a}{2U_\infty^2}\cos(\alpha+\theta) = \frac{3l_a C_M}{2t_a I^*} \qquad (1.11)$$

In the above equation, t_a is the flap thickness and I^* is the ratio of the flap moment of inertia to the moment of inertia of the equivalent fluid, which simplifies to the ratio of the flap density to the fluid density $\left(\rho_a/\rho_f\right)$. Solutions to equation (1.11) are obtained by decomposing it into a set of two, coupled, first-order ODEs and applying a third-order Runge-Kutta scheme, as implemented by Apte et al.

Airfoil Model

In this study, the dimensions of the wing and flap are those of an existing physical prototype. The chord length is 20 cm $(c = 0.2m)$; the flap represents 30% of the chord length $(l_a = 0.06m)$; and the airfoil is 2% thick $(t_a = 0.004m)$. Figure 3 shows an annotated CAD rendering of the physical model.

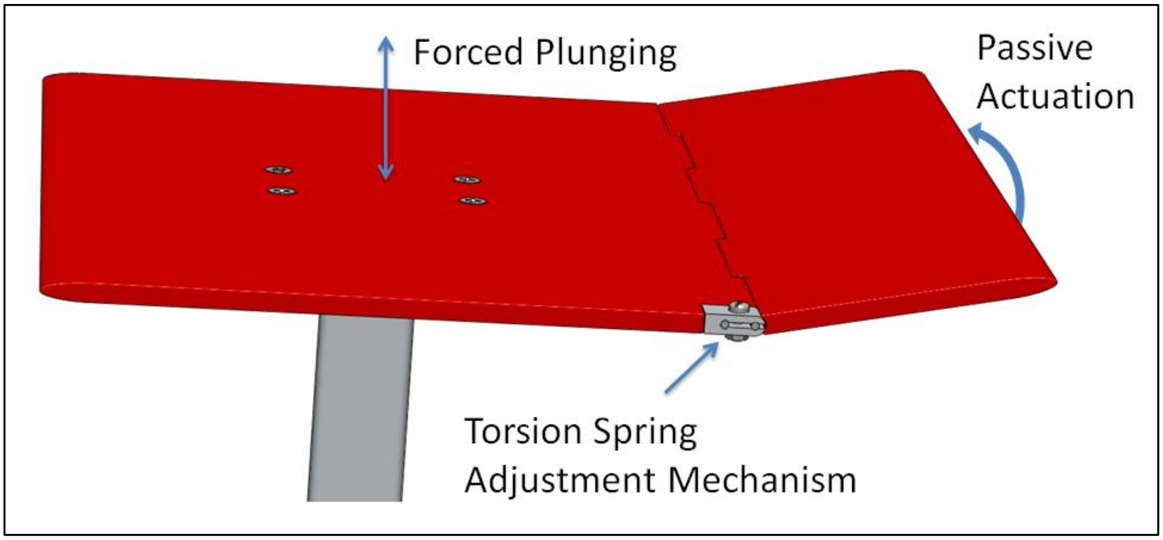

Figure 3: 3D CAD model of the physical wing prototype. The wing features an adjustable torsion spring system to facilitate analysis of the spring stiffness parameter. A vertical mounting post positions the trailing edge away from the sting balance.

The current model is slightly different than that used by Apte and Drost, differing in its thickness-to-chord ratio of 0.02 versus 0.038 for the older model. The wing is modeled in the solver as a two-dimensional collection of surface points, connected to form a simplified surface profile. The method used to generate the surface points is outlined in the report by Drost [3].

IMPLEMENTATION

Grid Refinement Study

To identify an adequate grid resolution, several cell sizes were investigated. A Cartesian grid that spanned 30 times the diameter of the cylinder in the x- and y-directions was used, with a uniform refinement patch centered on the cylinder to ensure a well-resolved surface. Three different cell sizes were used to calculate the flow past a stationary cylinder. Grid sizes of 100 by 100, 200 by 200, and 400 by 400 were used, each with 50 percent of the x-direction and y-direction cells occupying the refinement region. The cell spacing within the refinement region corresponded to grid resolutions of D/17, D/33, and D/67, respectively. The remaining cells were gradually stretched away from the cylinder using a hyperbolic tangent function.

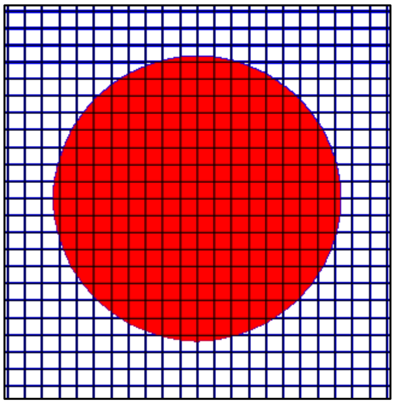

Figure 4: Uniform refinement patch for 100 by 100 (D/17) grid. Two other grids of double and quadruple the resolution shown were also studied.

Two cells span the z-direction, with periodic boundary conditions. Tests were performed at a Reynolds number of 200, based on the cylinder diameter. Strouhal numbers were calculated for each case by $St = \frac{f*D}{U_\infty}$, where f represents the respective vortex shedding frequency (obtained from the plots of lift and drag coefficients). Table 1 lists the Strouhal numbers obtained from each grid spacing (example calculations in Appendix B).

Grid Size	100 by 100 (D/17)	200 by 200 (D/33)	400 by 400 (D/67)
Strouhal Number	0.1969	0.1953	0.1984

Table 1: Strouhal number per grid resolution for static cylinder cases at Re=200. Interestingly, the results for the D/17 grid are more similar to the D/67 results than are the D/33 results. It was expected to see consistent trend, and the reason for this discrepancy not entirely clear.

Qualitatively, the flow behavior around the cylinder can be visualized as vorticity contours. Figure 5 shows temporal out-of-phase vorticity contours that are shedding from the cross-stream cylinder at a Reynolds number of 200.

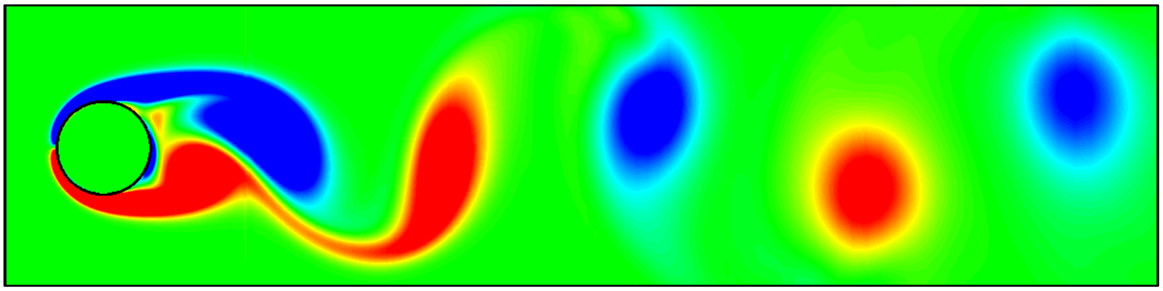

Figure 5: Temporal out-of-phase vorticity contours for a cylinder in a cross-flow. Grid size = 400 by 400 (D/67).

Apte [2] identified 0.1986 as an adequate Strouhal number for this specific case, which matches well with the Strouhal number calculate from the present D/67 test grid. Figure 6 and Figure 7, below, show the cylinder lift and drag coefficients for each grid resolution.

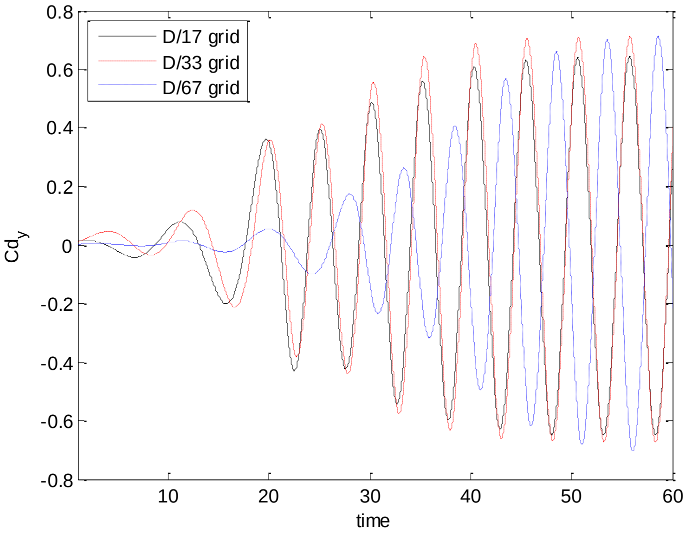

Figure 6: Lift coefficient comparison for different static cylinder grid resolutions. A dramatic difference is observed when a grid resolution of D/67 is used.

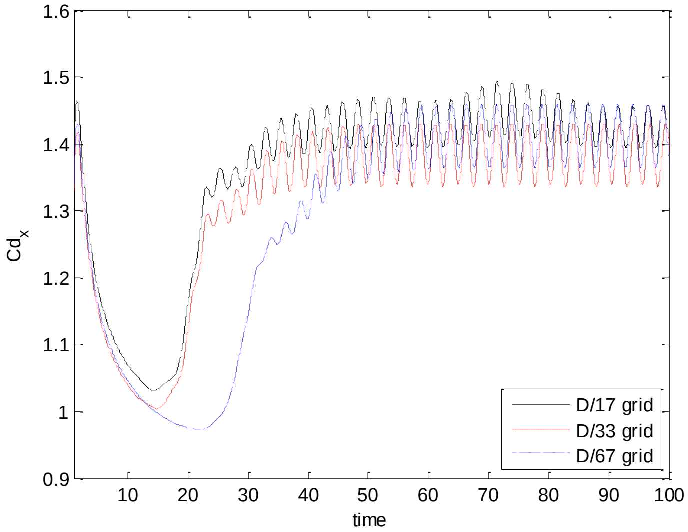

Figure 7: Drag coefficient comparison for different static cylinder grid resolutions. Again, a clearly nonlinear trend is observed from one resolution to the next.

Verification Tests

The fluid-structure interaction solver was verified by simulating flow past a spring-mounted cylinder with two degrees of freedom, and comparing the results to established data. The finest grid used in the refinement study (D/67) was again used for the dynamic cylinder case. The natural frequency of the spring-mass system was set based on the Strouhal number (Table 1), calculated from the corresponding static cylinder vortex shedding frequency. The figure below illustrates the situation to be studied, which is a two-dimensional spring-mass-damper system in a cross-flow.

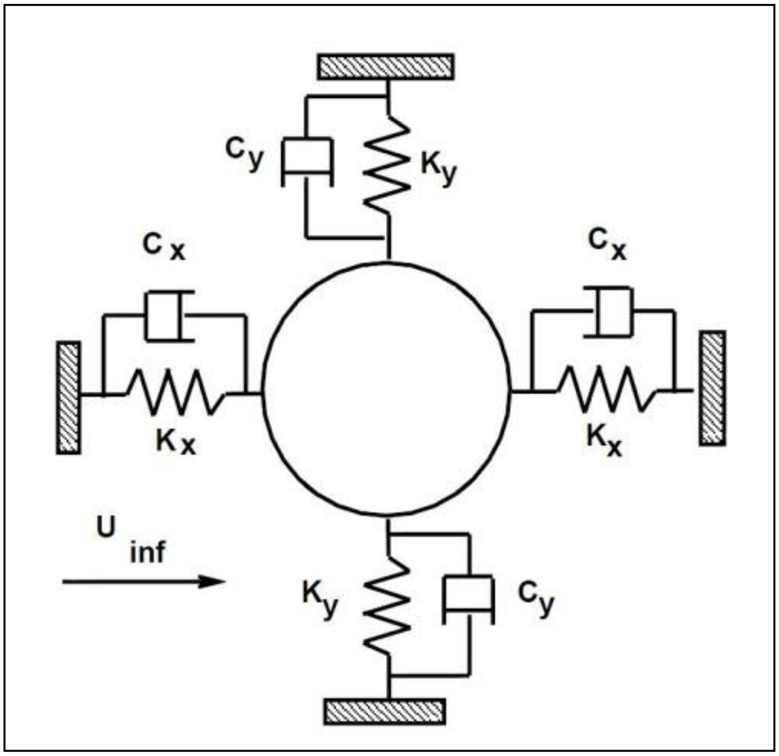

Figure 8: Diagram of spring-mounted cylinder with two degrees of freedom. Angular rotations of the springs were not taken into consideration. Source: [8]

Three cases were run with the damping factor (xi) varied from 0.001 to 0.1 (two orders of magnitude). Figure 9 shows the cross-stream displacements calculated by Apte, using the same solution algorithm as the present study, in comparison to published data by Blackburn & Karniadakis [12]. The current scheme yields excellent prediction capabilities compared to these studies.

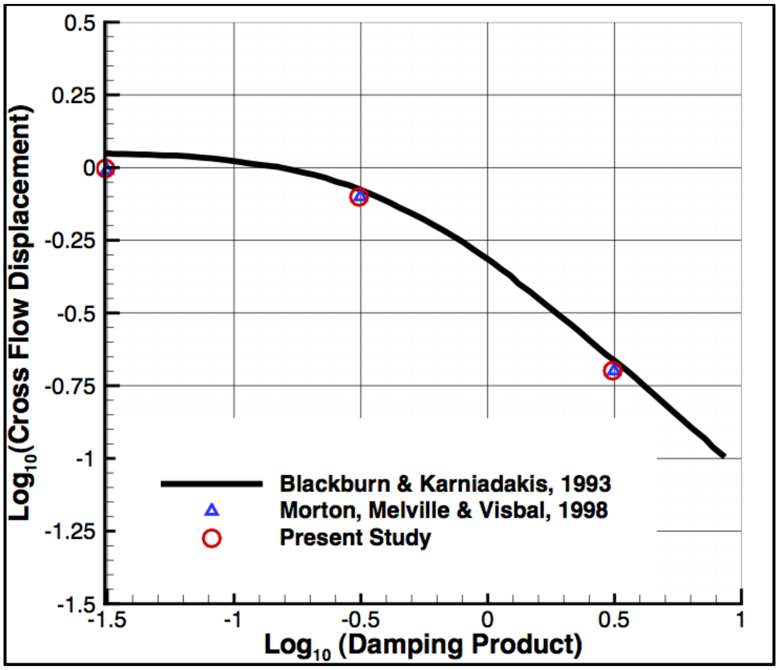

Figure 9: Cross-stream displacement obtained by Apte [2] in comparison with published data by Blackburn et al [12].

Flow over a Plunging Airfoil with Passively Actuated Tail Flap

The thin, flat, airfoil was subjected to a simple sinusoidal plunging motion of frequency 10 Hz and amplitude 1 cm (equal to 5% of the chord length). Cases were run at an angle of attack of 5 degrees and a Reynolds number of 1000. The free-stream velocity was set to 1 m/s, and the fluid density to 1 kg/m^3. A Reynolds number of exactly 1000 was achieved by setting the fluid viscosity to 0.0002 m^2/s. The length of the passive trailing-edge flap was equal to 30% of the total chord length. The chord length was 20 cm and the airfoil thickness was 4 mm (2%). Figure 10, below, illustrates this setup.

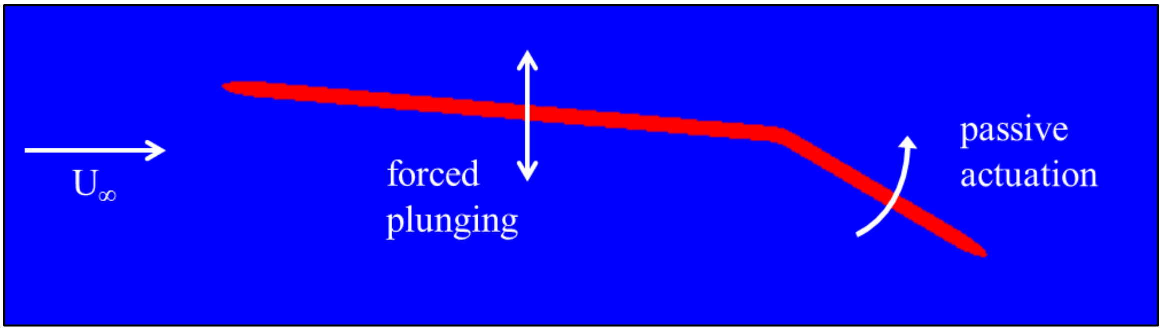

Figure 10: Computational representation of a thin airfoil with a trailing-edge flap.

First, a case was run with a static flap fixed parallel to the wing, to observe a baseline scenario of a simple plunging flat plate. Five cases were then run with the flap allowed to passively actuate. The airfoil model was positioned within a uniform grid refinement patch, large enough to contain the oscillatory motions. A cell size of $t_a/10$ was used in the refinement area to ensure a well-resolved wing surface (see Figure 11, below).

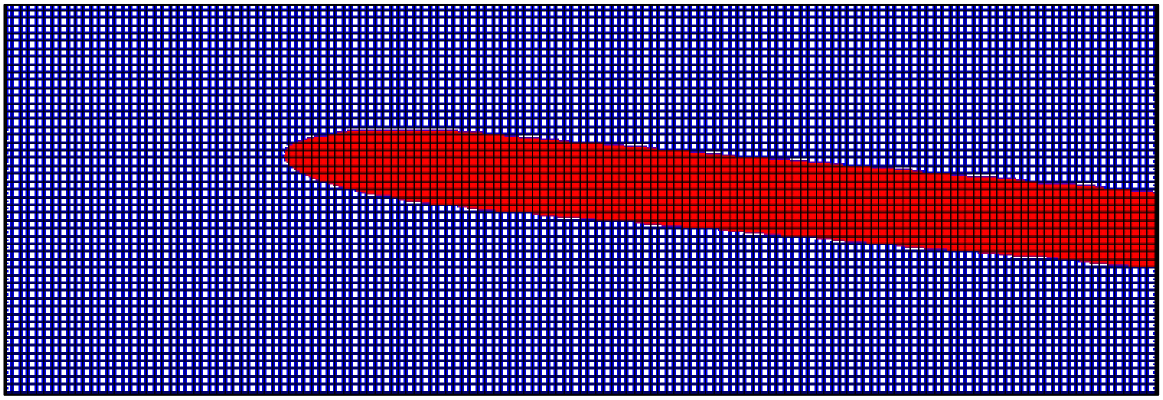

Figure 11: Uniform grid region over leading edge of airfoil. Cells in red region are considered to be within the airfoil, and are therefore constrained to rigid body motion.

Outside of the refinement patch, the cells were gradually stretched away using a hyperbolic tangent function. The amplitude and frequency of plunging was identical for each case. For comparison with the work by Apte, the natural frequency of the spring-flap system was varied to produce symmetric frequency ratios about the resonance case. Where f represents the frequency of plunging (10 Hz) and f_N represents the natural frequency. Specific ratios of $f / f_N = 0.5,\ 0.8,\ 1.0,\ 1.25, \text{ and } 2.0$ were studied, as well as the static flap scenario $\left(f / f_N = 0 \right)$. Each case was allowed to run for 10-12 periods of oscillation to allow any transient behavior to dissipate. The latter 6 periods of stable behavior were then used to calculate average values of lift and drag coefficients. An even number of periods were used because it was observed that the oscillations in lift and drag coefficients demonstrated alternating cycle variations.

RESULTS

As the airfoil underwent a sinusoidal plunging motion, the lift and drag characteristics along with many other parameters were monitored. Table 2 summarizes the average lift and drag forces as a function of the frequency ratio. The amplitude ratio of the trailing-edge oscillation to the leading-edge oscillation, as well as the propulsive efficiency, is also listed in the table. To calculate the propulsive efficiency, the following definition was used:

$$\eta = -\frac{\overline{F_D} U_\infty}{\overline{F_L v}} \qquad (12)$$

The negative sign is used to compensate for the negative drag force. In equation (12), v represents the vertical velocity of the airfoil as a result of the forced plunging motion. Equations (13) and (14) give the functions for the plunging motion and the vertical velocity, respectively, noting that the vertical velocity is merely the time derivative of the plunging motion.

$$y = 0.05c * \sin(2\pi f * t) \qquad (13)$$

$$v = \dot{y} = 0.05c * 2\pi f * \cos(2\pi f * t) \qquad (14)$$

To calculate the amplitude ratio, the leading-edge oscillation amplitude was defined as the amplitude of the plunging waveform. The trailing-edge amplitude was found by calculating the displacement distance of the trailing edge relative to the zero-position (parallel to the wing). The equation of the trailing-edge displacement is given in equation (15), where l_a represents the flap length, and θ is the flap displacement angle.

$$y_{TE} = l_a * \sin(\theta) \qquad (15)$$

f/f_N	a_{TE}/a_{LE}	η	$\bar{C}_{prop}$	$\bar{C}_D$	$\bar{C}_L$	Flap $\bar{C}_D$	Flap $\bar{C}_L$
0 (static)	1	0.023	1.475	-0.033	0.667	-0.154	-0.021
0.5	0.2305	-0.004	1.667	0.007	0.628	-0.114	-0.023
0.8	1.159	-0.066	2.253	0.147	0.929	0.084	0.057
1	2.653	0.150	0.773	-0.114	0.930	-0.141	0.089
1.25	1.138	0.210	0.782	-0.162	0.653	-0.280	-0.003
2	0.7902	0.136	0.977	-0.130	0.747	-0.247	0.006

Table 2: Summary of airfoil average lift and drag coefficients, as a function of frequency ratio. a_{TE}/a_{LE} is the ratio of the oscillation amplitude of the trailing edge over the leading edge, and η is the propulsive efficiency of the airfoil.

As expected, the resonance case produced the largest flap displacements (as indicated by the amplitude ratio in column 2). The most noteworthy trend, however, would be the negative drag coefficients seen at frequency ratios equal to or greater than 1, and also for the static flap case. One might also notice that mean drag coefficient values for the flap by itself share a similar trend with the overall drag coefficients, but with an extra negative value at $f/f_N=0.5$. Looking at the corresponding overall drag coefficient for that case, the $\overline{C_D}$ value appears to be almost zero in comparison with the other drag coefficients (approximately 2 orders of magnitude smaller). This indicates that the $f/f_N=0.5$ case is on the verge of producing a positive thrust value, which makes sense given its behavioral similarity to the static flap case (see Table 3, below). In comparing the drag coefficients of the passive flap cases to that of the static flap case (to identify any benefits of passive actuation), it is noticed that the drag coefficient of the static case is roughly zero, in comparison with many of the values obtained from the dynamic flap cases. Therefore, it can be concluded that the addition of a passively-actuated tail flap does produce measureable differences. Given the proper combination of the plunging frequency and natural frequency, these differences can be quite advantageous.

Thus far, the quantitative effects of the passively actuated trailing-edge flap have been examined. It is also informative to observe the qualitative behavior of the airfoil under the circumstances in which it was simulated. Looking at Table 3, the flow patterns around the airfoil are clearly visible as vorticity contours. The table is situated such that phases of plunging are listed horizontally, and the different cases of plunging frequency over natural frequency are presented on different rows. Clear trends and patterns are visible in the data.

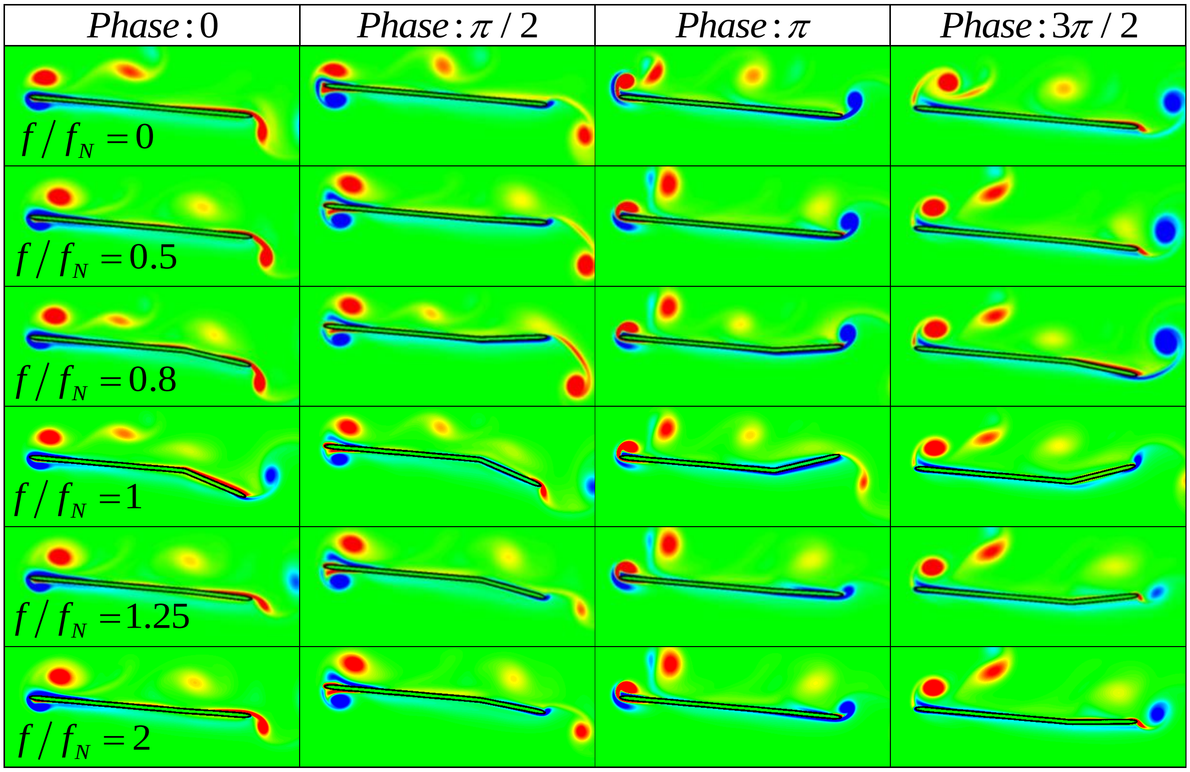

Table 3: Vorticity contours for airfoil plunging scenario. Phase 0 is the center position going up. Phase pi/2 is the upper-most position. Phase pi is the center position going down. And phase 3pi/2 is the lower-most position.

A major aspect of the vorticity contours seen in Table 3 is their comparatively smooth behavior, when compared with the vorticity contours generated by Apte [2]. This is certainly to be expected, since the cases in this study are at a much lower Reynolds number. The plots in Table 3 also show that the oscillation of the flap about its mean position is out of phase with the plunging motion for frequency ratios greater than 1. In other words, for those cases, the flap is above its mean position when the plunge is below the midline, and the flap is below its mean position when the plunge is above its midline. Conversely, the lower frequency ratios seem to be more or less in phase with the plunging motion. These concepts are further illustrated in Figure 12 and Figure 13. In the following figures that illustrate flap position, it should be noted that the flap displacement angle is measured positive counter-clockwise. That is, a positive θ value indicates a flap that is above the mean position.

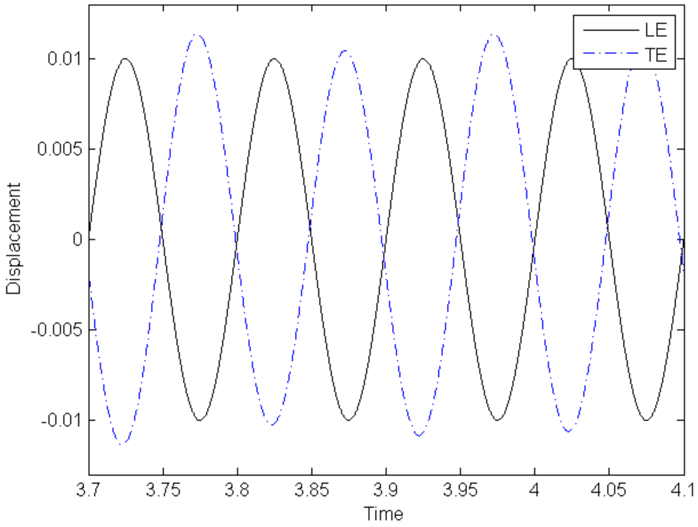

Figure 12: Plunging waveform versus flap displacement, $f/f_N=1.25$.

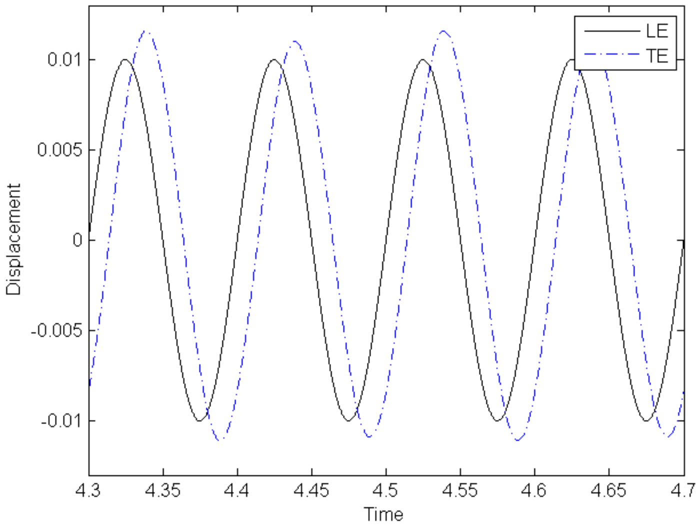

Figure 13: Plunging waveform versus flap displacement, $f/f_N=0.8$.

The previous two figures show comparisons of the plunging motion and the flap displacement for the maximum thrust case ($f/f_N=1.25$) and its reciprocal ($f/f_N=0.8$). These plots show how the larger frequency ratio produces flap displacements that attempt to counter the motions of the plunging, whereas the lower ratio actuation adds to the plunging motion. Appendix E lists similar plots for all cases examined, and it can be seen through these figures that frequency ratios less than 1 tend to produce flap actuation that is between 0 and 90 degrees ahead of the plunging waveform, and ratios larger than or equal to 1 produce actuation that is between 90 and 180 degrees ahead. Plotting the phase shift for each case versus the respective frequency ratio yields a sigmoidal curve tapering off at 180 degrees. From Figure 14, it can be seen that the beneficial effects are obtained at phase shifts greater than 90 degrees.

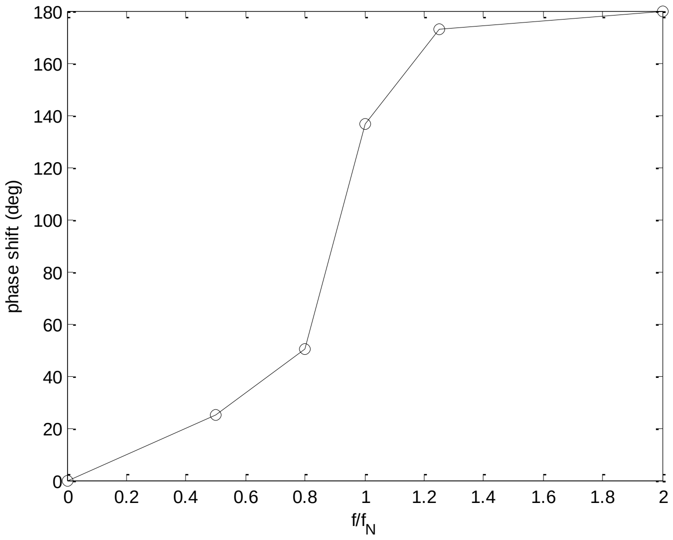

Figure 14: Trailing-edge flap phase shift relative to the plunging waveform.

Figure 15 and Figure 16 give a comparative view of the motion of the leading edge and trailing edge, over a graph of power input for plunging. Note that the vertical scale of C_{prop} been adjusted for easy comparison. In comparing the two figures a distinct upward shift of the power input can be noticed, owing to the opposite behavior of the flap (out of phase vs. in phase). This explains the poor propulsive efficiencies of the lower frequency ratios. An examination of the drag profile should confirm this.

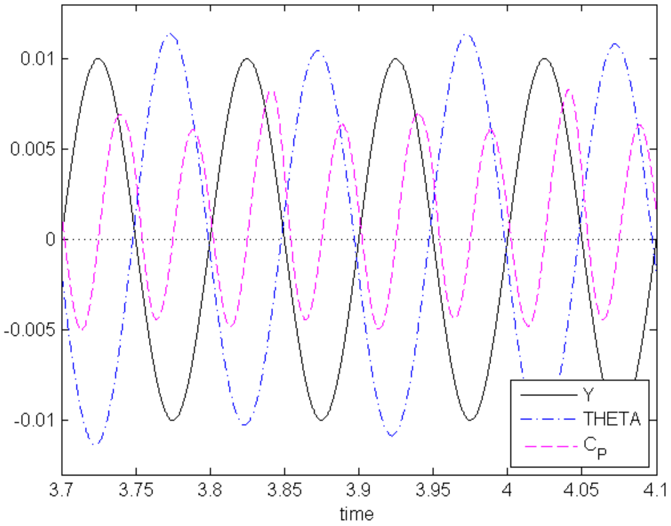

Figure 15: Comparison of plunging waveform, flap displacement and power input for a frequency ratio of $f/f_N=1.25$. C_{prop} *values scaled by factor of 0.0015 for clarity.*

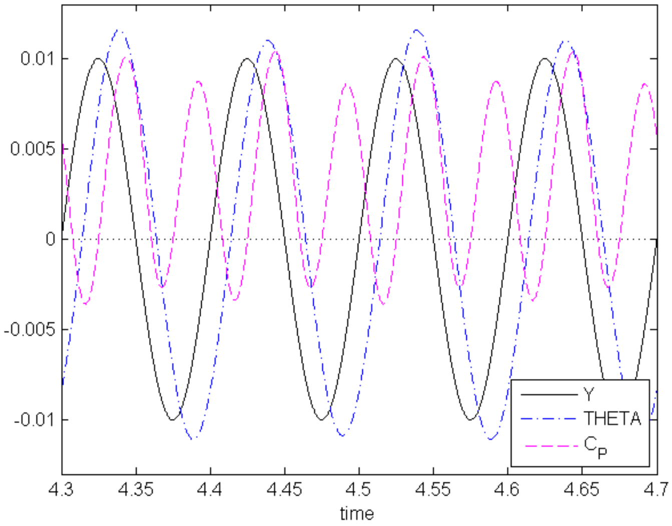

Figure 16: Comparison of plunging waveform, flap displacement and power input for a frequency ratio of $f/f_N=0.8$. C_{prop} *values scaled by factor of 0.0015 for clarity.*

Looking at the drag characteristics in comparison with the plunging and actuation behavior, Figure 17 and Figure 18 show how the behavior of the tail flap affects the drag on the airfoil.

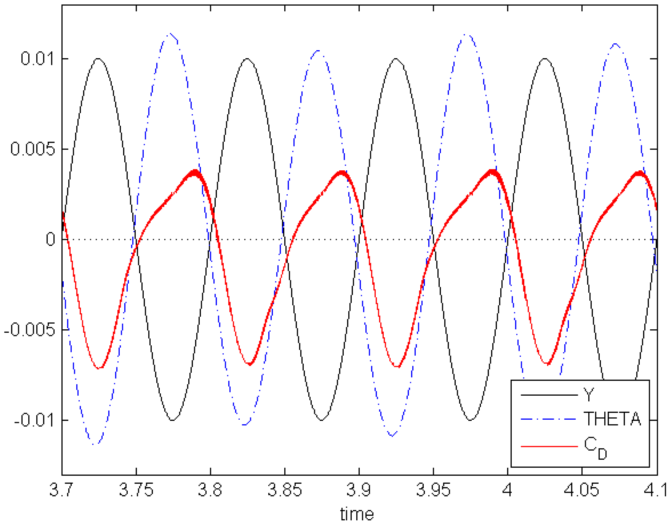

Figure 17: Comparison of plunging waveform, flap position, and drag coefficient, for f/f_N*=1.25. Note: The drag coefficient is scaled by a factor of 0.005 for ease of analysis.*

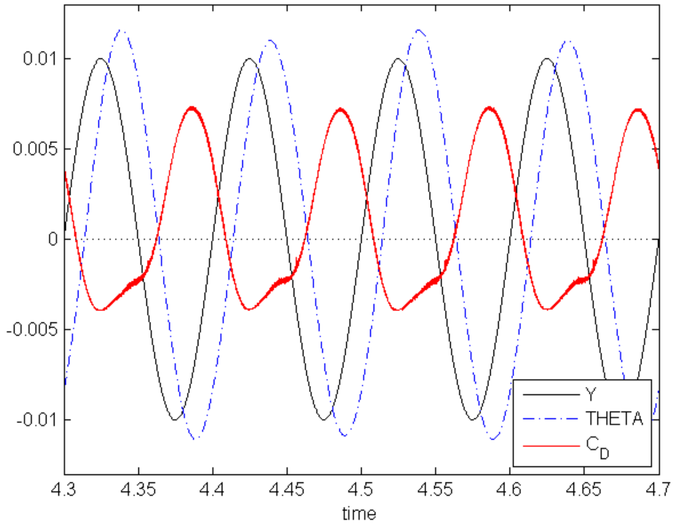

Figure 18: Comparison of plunging waveform, flap position, and drag coefficient, for $f/f_N=0.8$*. Note: The drag coefficient is scaled by a factor of 0.005 for ease of analysis.*

In contrast, Figure 19 shows the drag coefficient and plunging position for the case of a static flap.

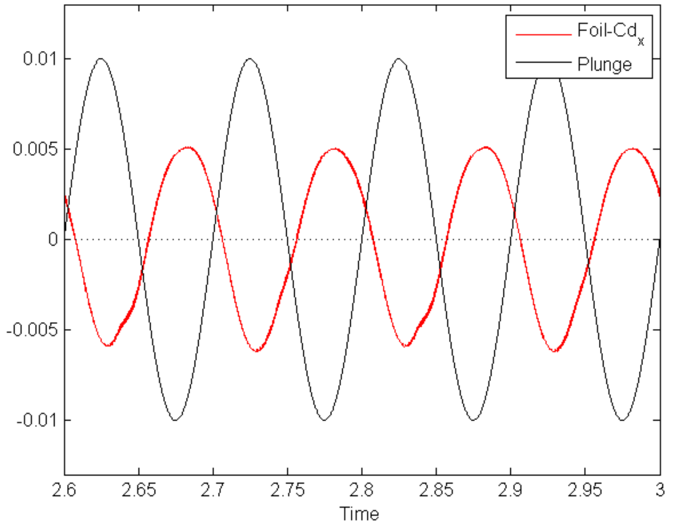

Figure 19: Comparison of plunging waveform and drag coefficient for $f/f_N=0$*. Note: The drag coefficient is scaled by a factor of 0.005 for ease of analysis.*

Between the high and low frequency cases, it is immediately apparent that the drag coefficient is skewed downward for the larger frequency ratio, and skewed upward for the smaller ratio. This indicates a decrease in drag for the larger frequency ratio. Figure 17 through Figure 19 are further broken down by phase in the following analysis.

- *Phase 0:* In this position, the airfoil is at the midline of its plunge and about to go up. For f/f_N=1.25, it is observed that flap position is essentially zero, and the drag is positive and decreasing. In the case of no actuation, the drag value is also positive and decreasing. For f/f_N=0.8, the flap is below the mean position and the drag coefficient is again positive.
- *Phase π/2:* Here, the plunging position is at its maximum positive value and the drag coefficient is almost at its minimum (producing thrust) for all three cases. For f/f_N=0.8, the flap angle is near its most positive value above the mean position. The flap is near its lowest position for the f/f_N=1.25 case.
- *Phase π:* In this stage, the airfoil is in the center-most position of the plunging cycle about to go downward. Drag values are negative (thrust) and increasing toward zero for all three cases plotted above. In the case of f/f_N=0.8, the flap angle is largely above the mean position and decreasing. For f/f_N=1.25, the flap is approximately at the mean position and increasing.
- *Phase 3π/2:* Lastly, this phase represents the airfoil at its lowest plunging position. For each case, the drag value is at its largest positive value (or very near). The f/f_N=0.8 case yields a flap angle below the mean position, and f/f_N=1.25 shows a flap that is well above the mean position.

The seemingly opposite behavior of the passive flap between cases where $f/f_N > 1$ and $f/f_N < 1$, appears to have the net effect of producing thrust at the higher frequency ratios. This could be explained by observing the trailing-edge vortex shedding behavior between the different cases studied. The two most extreme examples are highlighted below.

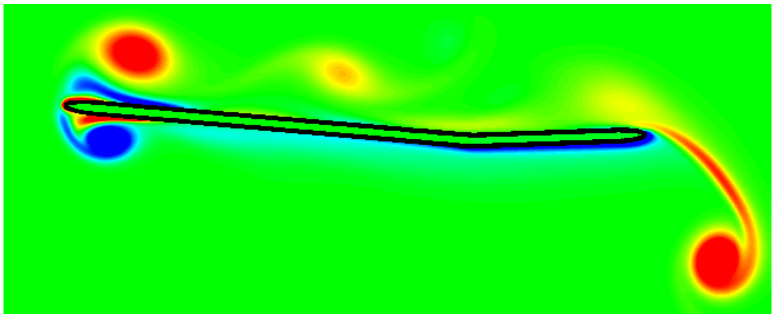

Figure 20: Vortex shedding behavior at phase π/2 for $f/f_N=0.8$.

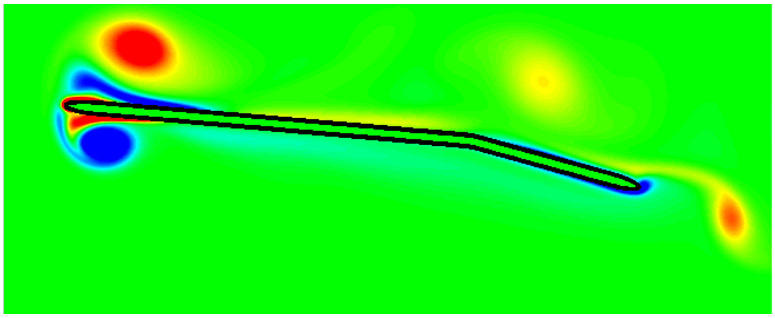

Figure 21: Vortex shedding behavior at phase π/2 for $f/f_N=1.25$.

Besides the opposite position of the passive flap in these two figures, the most obvious difference would be the magnitude differences of the trailing-edge vortices. In the $f/f_N=0.8$ case, the vortex is much greater, owing to the fact that the compounded effect of a rising airfoil plus a rising flap is more capable of disturbing the trailing-edge fluid. The energy required to generate the larger vortex would translate into a larger drag force for the case of an in-phase flapping motion. This is confirmed by fact that, at this particular instant, the out-of-phase flap is producing twice the amount of thrust as the in-phase flap.

In summary, the out-of-phase motions for frequency ratios greater than or equal to 1 tend to allow the flap to be less of a disturbance to the trailing-edge fluid, thereby increasing the overall thrust value for these cases.

SUMMARY AND FUTURE WORK

The effects of a spring-mounted passively actuated trailing-edge flap were modeled in two dimensions using a fictitious domain method by Apte et al. The airfoil studied was similar to that of Apte [2] and Drost [3], but with a smaller thickness-to-chord ratio to accommodate new project goals. The airfoil was subjected to a sinusoidal plunging motion to simulate a flapping wing, and cases were run at a Reynolds number of 1000. It was shown by the drag values in Table 2 that the presence of a passively actuated trailing-edge flap does produce beneficial results, provided that the proper ratio of the plunging frequency and natural frequency is obtained. Specifically, natural frequencies lower than or equal to the plunging frequency were shown to produce thrust, rather than drag. Thrust was also produced with a rigid flap, that was fixed parallel to the wing, implying that a plunging flat-plate airfoil has the potential to generate thrust without the aid of a passive flapping mechanism. However, the thrust value for the fixed flap scenario was nearly zero in comparison to the large-frequency-ratio passive-actuation cases, suggesting that the presence of a passive flap may provide much greater performance.

Comparing the performance of this airfoil, at a Reynolds number of 1000, to the performance of the similar airfoil simulated by Apte, at a Reynolds number of 14700, reveals an opposite trend in drag performance versus frequency ratio. Table 4 lists the results obtained by Apte for this situation.

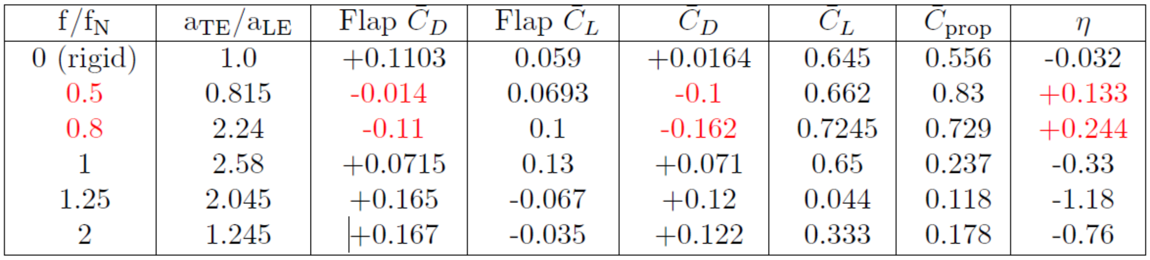

f/f_N	a_{TE}/a_{LE}	Flap $\bar{C}_D$	Flap $\bar{C}_L$	$\bar{C}_D$	$\bar{C}_L$	$\bar{C}_{\text{prop}}$	η
0 (rigid)	1.0	+0.1103	0.059	+0.0164	0.645	0.556	-0.032
0.5	0.815	-0.014	0.0693	-0.1	0.662	0.83	+0.133
0.8	2.24	-0.11	0.1	-0.162	0.7245	0.729	+0.244
1	2.58	+0.0715	0.13	+0.071	0.65	0.237	-0.33
1.25	2.045	+0.165	-0.067	+0.12	0.044	0.118	-1.18
2	1.245	+0.167	-0.035	+0.122	0.333	0.178	-0.76

Table 4: Results obtained by Apte [2], for a low-Reynolds-number plunging airfoil, with a passively actuated trailing-edge flap, very similar to the present study. Highlighted in red are the cases that produced thrust, rather than drag.

The main differences between the past and present study are 1) the Reynolds number at which the tests were performed, and 2) the thickness-to-chord ratio of the wings being tested. The plunging amplitudes, plunging frequencies, and frequency ratios were the same for both cases. A major difference in the behavior of the spring-mounted trailing-edge flaps for the different studies was the phase shift of the different cases. As Apte observed, the best performance was obtained when the trailing-edge flap was 90° out-of-phase with the leading edge. The present study shows that the highest propulsive efficiency and largest thrust are obtained when the trailing edge is 180° out-of-phase. Reasons for this discrepancy in beneficial phase shift may stem from the different time scales of flow past the wings, resulting different interactions between the shedding leading-edge vortices and the flap position. For the frequency ratio of 1.25, the 180° out-of-phase motion of the trailing edge, in the present study, results in a flap center-of-rotation located almost exactly on the trailing edge (meaning that the trailing edge remains almost stationary as a result of the opposite motions of the flap and the plunging). This may be the reason that the frequency ratio of 1.25 yields the best performance.

Future plans are already in progress for the next phase of studying the effects of passive flap actuation on thin airfoils. A possible experiment could be the simulation of a thin airfoil with passively actuated flaps on both the leading and trailing edges at the same time. Complex combinations of leading-edge and trailing-edge spring frequencies could be studied, as well as different flap lengths. A conceptual model of such an airfoil is shown below, in Figure 22.

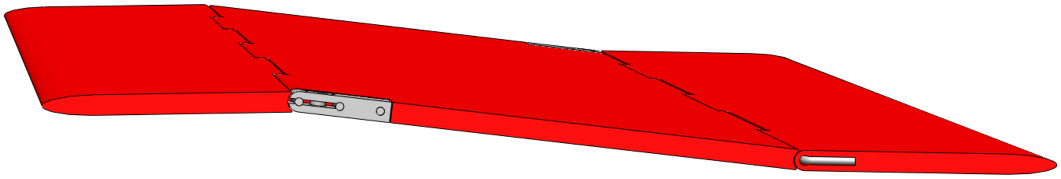

Figure 22: A conceptual CAD model of a thin airfoil with a passively actuated flap on both the leading edge and trailing edge. This type of setup may provide more information as to the nature of drag in relation to passive actuation.

REFERENCES

[1] S. Apte, M. Martin and N. Patankar, "A Numerical Method for Fully Resolved Simulation (FRS) of Rigid Particle–Flow Interactions in Complex Flows," *Journal of Computational Physics,* vol. 228, p. 2712–2738, 2009.

[2] S. V. Apte, "Low Reynolds Number Flow Dynamics and Control of a Pitching Airfoil with Elastically Mounted Flap Actuator," 2011.

[3] K. J. Drost, "Direct Numerical Simulation of a Flat Wing with a Movable Front Flap at High Angles of Attack and Low Reynolds Numbers," 2010.

[4] G. McCullough and D. Gault, "Examples of Three Representative Types of Airfoil-Section Stall at Low Speed," 1951.

[5] K. Taira and T. Colonius, "Three-Dimensional Flows Around Low-Aspect-Ratio Flat-Plate Wings at Low Reynolds Numbers," *Journal of Fluid Mechanics,* vol. 623, pp. 187-207, 2009.

[6] D. Kim and H. Choi, "Immersed boundary method for flow around an arbitrarily moving body," Journal of Computational Physics, 2006.

[7] A. Uranga, P.-O. Persson, M. Drela and J. Peraire, "Implicit Large Eddy Simulation of Transitional Flows Over Airfoils and Wings," no. AIAA 2009-4131, 2009.

[8] J. Alonso, L. Martinelli and A. Jameson, "Multigrid Unsteady Navier-Stokes Calculations with Aeroelastic Applications," 1995.

[9] H. Masoud and A. Alexeev, "Resonance of flexible flapping wings at low Reynolds

number," Physical Review, 2010.

[10] A. Broeren and M. Bragg, "Unsteady Stalling Characteristics of Thin Airfoils at Low Reynolds Number," in *Fixed and Flapping Wing Aerodynamics for Micro Air Vehicle Applications*, 191-213, American Institute of Aeronautics & Astronautics, 2001.

[11] M. Visbal, R. Gordnier and M. Galbraith, "High-Fidelity Simulations of Moving and Flexible Airfoils at Low Reynolds Numbers," *Experimental Fluids,* vol. 46, pp. 903-922, 2009.

[12] H. M. Blackburn and G. E. Karniadakis, "Two- and Three-Dimensional Simulations of Vortex-Induced Vibration of a Circular Cylinder," 1993.

[13] J. Yang, S. Preidikman and E. Balaras, "A Strongly Coupled, Embedded-Boundary Method for Fluid-Structure Interactions of Elastically Mounted Rigid Bodies," *Journal of Fluids and Structures,* vol. 24, pp. 167-182, 2008.

APPENDICES

Appendix A: Grid Resolutions for Static and Dynamic Cylinder Cases

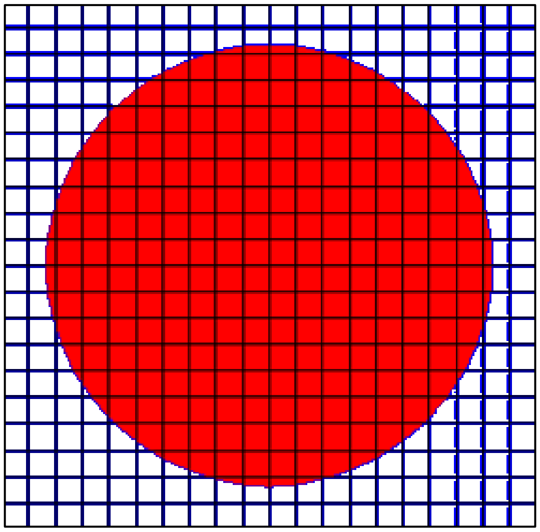

Figure A 1: Uniform refinement patch for D/33 grid.

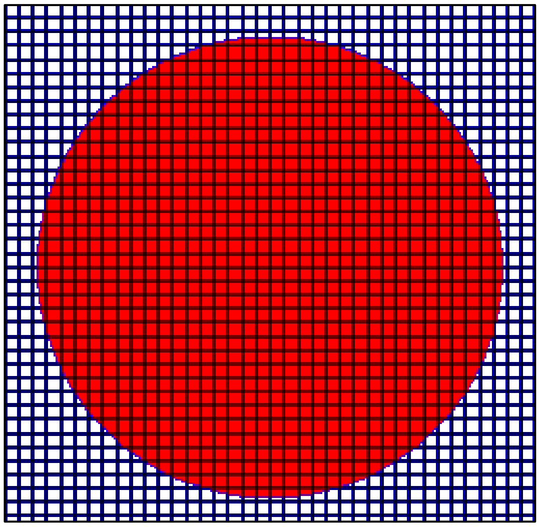

Figure A 2: Uniform refinement patch for D/33 grid.

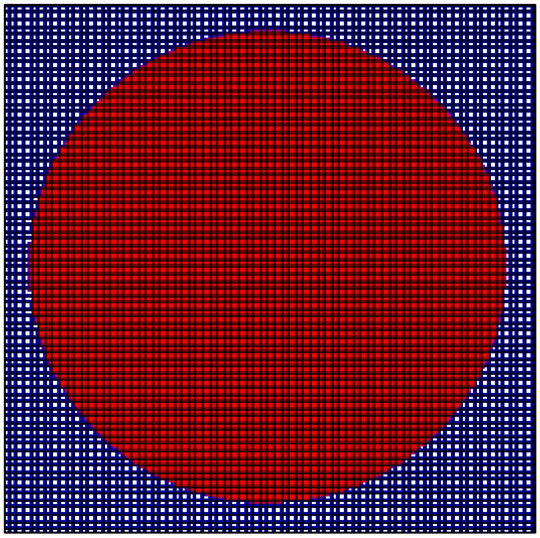

Figure A 3: Uniform refinement patch for D/67 grid.

Appendix B: Strouhal Number Calculations for Flow past a Stationary Cylinder

To calculate the Strouhal number of a cylinder in a cross flow, the oscillatory frequency of the lift coefficient was measured and averaged over 10 periods. This frequency was then used in the equation $St = \frac{f*D}{U_\infty}$ to calculate the Strouhal number.

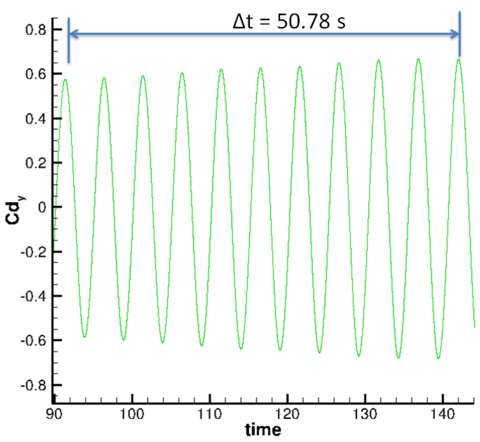

Figure A 4: Vortex shedding frequency measurement, D/17 grid.

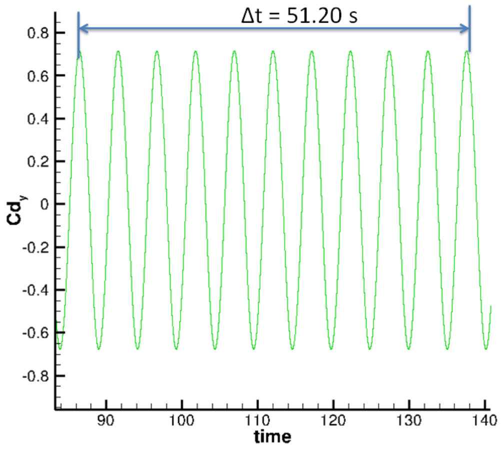

Figure A 5: Vortex shedding frequency measurement, D/33 grid.

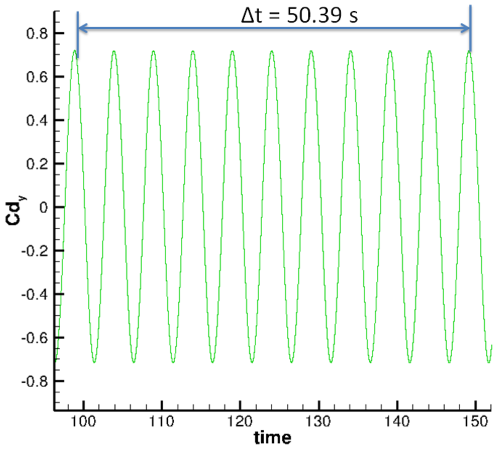

Figure A 6: Vortex shedding frequency measurement, D/67 grid.

Appendix C: C_D and C_L Plots for Static Cylinder Study

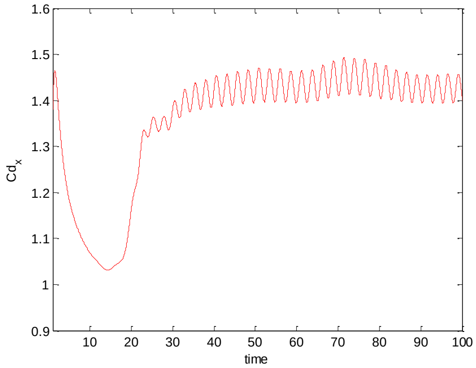

Figure A 7: Static cylinder drag coefficient for D/17 grid, Re=200.

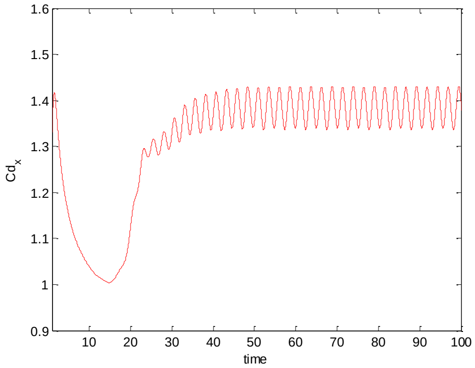

Figure A 8: Static cylinder drag coefficient for D/33 grid, Re=200.

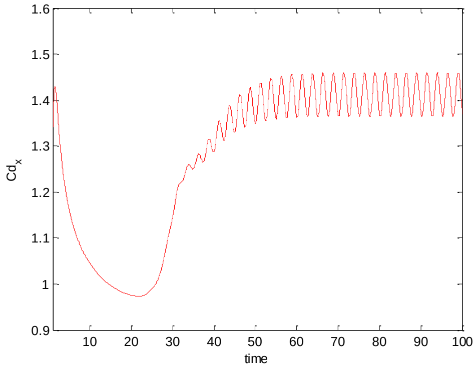

Figure A 9: Static cylinder drag coefficient for D/67 grid, Re=200.

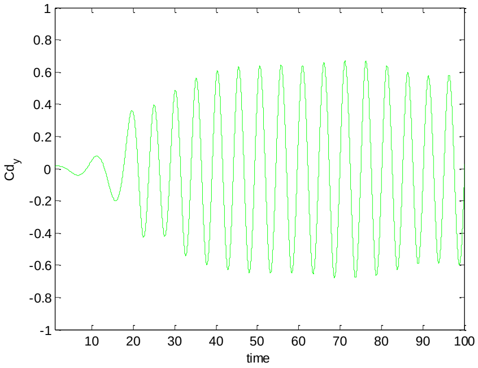

Figure A 10: Static cylinder lift coefficient for D/17 grid, Re=200, xi=0.001.

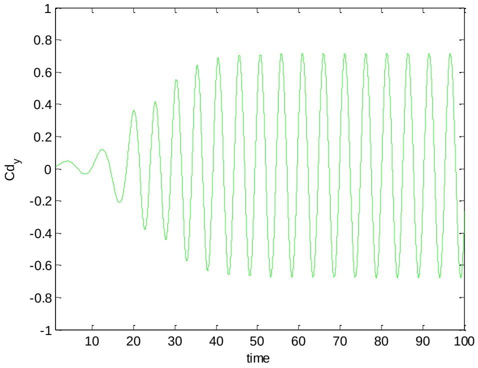

Figure A 11: Static cylinder lift coefficient for D/33 grid, Re=200, xi=0.001.

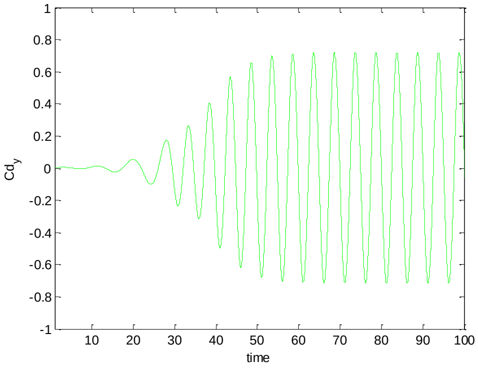

Figure A 12: Static cylinder lift coefficient for D/67 grid, Re=200, xi=0.001.

Appendix D: Cross-Stream Displacements for Spring-Cylinder Study.

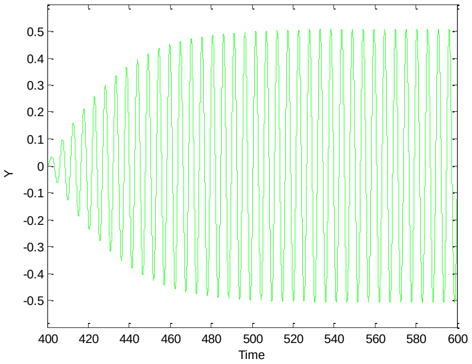

Figure A 13: Cross-stream displacement, D/67 grid, xi=0.001.

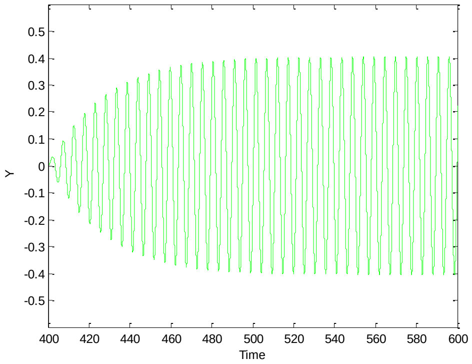

Figure A 14: Cross-stream displacement, D/67 grid, xi=0.01.

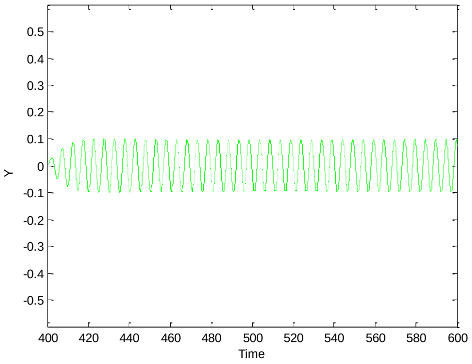

Figure A 15: Cross-stream displacement, D/67 grid, xi=0.1.

Appendix E: Comparison of Leading-Edge Amplitude to Trailing-Edge Amplitude.

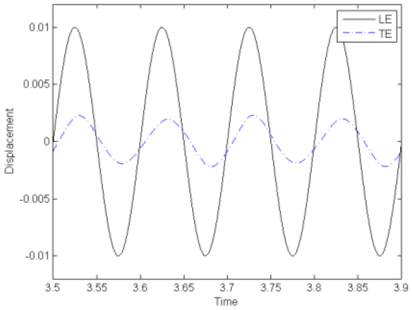

Figure A 16: Comparison of leading and trailing-edge waveforms, f/f$_N$=0.5.

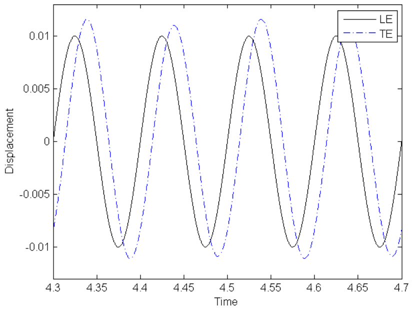

Figure A 17: Comparison of leading and trailing-edge waveforms, f/f$_N$=0.8.

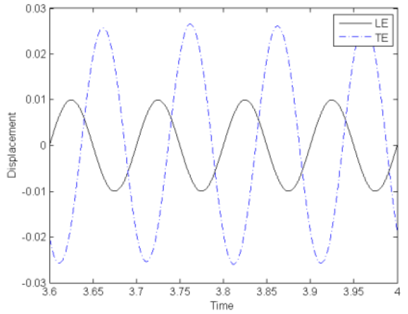

Figure A 18: Comparison of leading and trailing-edge waveforms, f/f$_N$=1.

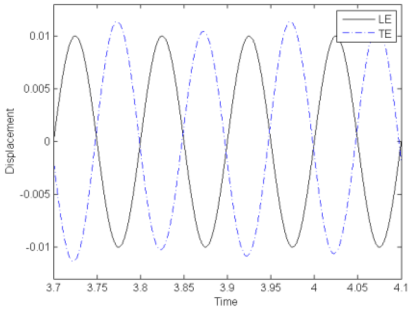

Figure A 19: Comparison of leading and trailing-edge waveforms, f/f$_N$=1.25.

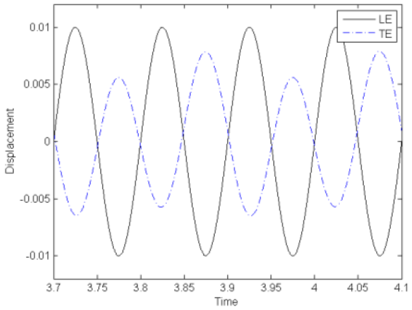

Figure A 20: Comparison of leading and trailing-edge waveforms, f/f$_N$=2.